Monthly Notices of the ROYAL ASTRONOMICAL SOCIETY

MNRAS **496,** 4674–4687 (2020) doi:10.1093/mnras/staa1882
Advance Access publication 2020 July 2

Simplified 3D GCM modelling of the irradiated brown dwarf WD 0137−349B

Graham K. H. Lee [1]★ Sarah L. Casewell,[2] Katy L. Chubb,[3] Mark Hammond,[1] Xianyu Tan [1] Shang-Min Tsai[1] and Raymond T. Pierrehumbert[1]

[1]*Atmospheric, Oceanic and Planetary Physics, Department of Physics, University of Oxford, Oxford OX1 3PU, UK*
[2]*Department of Physics and Astronomy, University of Leicester, University Road, Leicester LE1 7RH, UK*
[3]*SRON Netherlands Institute for Space Research, Sorbonnelaan 2, NL-3584 CA Utrecht, the Netherlands*

Accepted 2020 June 19. Received 2020 June 4; in original form 2020 January 17

ABSTRACT

White dwarf–brown dwarf short-period binaries ($P_{\rm orb} \lesssim 2$ h) are some of the most extreme irradiated atmospheric environments known. These systems offer an opportunity to explore theoretical and modelling efforts of irradiated atmospheres different to typical hot Jupiter systems. We aim to investigate the three-dimensional (3D) atmospheric structural and dynamical properties of the brown dwarf WD 0137−349B. We use the 3D global circulation model (GCM) Exo-Flexible Modelling System (FMS) with a dual-band grey radiative transfer scheme to model the atmosphere of WD 0137−349B. The results of the GCM model are post-processed using the 3D Monte Carlo radiative transfer model CMCRT. Our results suggest inefficient day–night energy transport and a large day–night temperature contrast for WD 0137−349B. Multiple flow patterns are present, shifting energy asymmetrically eastward or westward depending on their zonal direction and latitude. Regions of overturning are produced on the western terminator. We are able to reproduce the start of the system near-infrared (IR) emission excess at $\gtrsim$1.95 μm as observed by the Gemini Near-Infrared Spectrograph (GNIRS) instrument. Our model overpredicts the IR phase curve fluxes by factors of ≈1–3, but generally fits the shape of the phase curves well. Chemical kinetic modelling using VULCAN suggests a highly ionized region at high altitudes can form on the dayside of the brown dwarf. We present a first attempt at simulating the atmosphere of a short-period white dwarf–brown dwarf binary in a 3D setting. Further studies into the radiative and photochemical heating from the ultraviolet irradiation are required to more accurately capture the energy balance inside the brown dwarf atmosphere. Cloud formation may also play an important role in shaping the emission spectra of the brown dwarf.

Key words: radiative transfer – planets and satellites: atmospheres – stars: atmospheres – binaries: close – brown dwarfs – stars: individual: WD 0137−349B.

1 INTRODUCTION

Currently only a few post-common envelope, short-period white dwarf–brown dwarf (henceforth WD–BD) binary systems have been detected: GD 1400 (Farihi & Christopher 2004; Dobbie et al. 2005; Burleigh et al. 2011), WD 0137−349 (Burleigh et al. 2006; Maxted et al. 2006), WD 0837+185 (Casewell et al. 2012), NLTT 5306 (Steele et al. 2013), SDSS J141126.20+200911.1 (Beuermann et al. 2013; Littlefair et al. 2014; Casewell et al. 2018b), SDSS J155720.77+091624.6 (Farihi, Parsons & Gänsicke 2017), SDSS J1205−0242 (Parsons et al. 2017; Rappaport et al. 2017), SDSS J1231+0041 (Parsons et al. 2017), and EPIC 212235321 (Casewell et al. 2018a). Despite their rarity, with estimates of a ≈0.5 per cent rate of brown dwarf (BD) companions to white dwarfs (WDs; Steele et al. 2011), these systems offer a unique insight into the properties of irradiated atmospheres in more extreme conditions than typical hot Jupiter (HJ) systems.

The BD companion to WD 0137−349 was first inferred by Maxted et al. (2006) through high-resolution radial velocity measurements, finding a mass ratio of ≈0.134 for the system. Fitting the spectral data with a WD atmospheric model yielded a mass of ∼0.39 $M_\odot$, placing the companion in the BD mass regime at ∼53 $M_{\rm J}$. A near-infrared (near-IR) excess was also hinted at in archival Two Micron All-Sky Survey (2MASS; (Skrutskie et al. 2006) photometric data. Further observations using the Gemini Near-Infrared Spectrograph (GNIRS) instrument by Burleigh et al. (2006) confirmed the near-IR excess beyond ≈1.95 μm, providing a direct detection of the BD companion thermal emission. Casewell et al. (2015) performed a comprehensive observational campaign spanning the *V*, *R*, *I*, *J*, *H*, and K_s bands and also obtained *Spitzer* data for the 3.6, 4.5, 5.8, and 8 μm photometric bands. They presented phase curves for the BD companion, and calculated a day–night temperature contrast of $\gtrsim$500 K in most of the infrared (IR) bands. Longstaff et al. (2017) presented spectroscopic detections of Hα, He, Na, Mg, Si, K, Ca, Ti, and Fe emission from the BD companion, suggesting molecular dissociation occurring in the upper atmosphere of the BD.

Studying WD–BD binaries presents an opportunity to explore the nature of irradiated atmospheres in more 'extreme' conditions than typical HJ systems. Atmospheric modelling of the BD is a challenging prospect due to several factors.

★ E-mail: graham.lee@physics.ox.ac.uk

Table 1. Adopted physical parameters and derived characteristics of the WD 0137−349 system following Burleigh et al. (2006), Maxted et al. (2006), and Casewell et al. (2015).

$T_{\rm eff,\,WD}$ (K)	$R_{\rm WD}$ ($R_\odot$)	$M_{\rm BD}$ ($M_{\rm J}$)	$R_{\rm BD}$ ($R_{\rm J}$)	a ($R_\odot$)	$P_{\rm orb}$ (min)	Inc. (°)	Dist. (pc)
16500	0.019	53	1.1[a]	0.65	116	35	102

[a]Denotes an estimated value.

(i) Moderate irradiation from the WD ($T_{\rm eq} \approx$ 1000–2000 K), with >5 per cent of the stellar flux occurring at ultraviolet (UV) wavelengths.

(ii) High surface gravity ($g \gtrsim 1000$ m s^{-2}).

(iii) Fast rotational speeds ($P_{\rm orb} \lesssim 120$ min), assuming tidal locking.

Even when taken individually, these factors represent a significant regime change from typical HJ conditions. Examining these systems is therefore a test of current theories and models in a new context, and to provide the community with a holistic understanding of irradiated atmospheres.

In this initial study, we model the atmosphere of the companion BD in the WD 0137−349 system. We perform 3D global circulation models (GCMs) of the BD atmosphere with a simplified two-band grey radiative transfer scheme. The thermal structure of the GCM is then post-processed using a 3D radiative transfer code and compared to the observational data from Burleigh et al. (2006) and Casewell et al. (2015). In Section 2, we briefly review current atmospheric modelling efforts of WD–BD binaries and the dynamical expectations from previous HJ studies. Section 3 presents details of our GCM simulation and adopted parameters. Section 4 presents the results of our GCM simulation. Section 5 presents post-processing of our GCM simulation and comparison to available observational data. Section 6 presents the discussion of our results, and Section 7 contains the summary and conclusions.

2 PREVIOUS WD–BD MODELLING

To date, modelling efforts for WD–BD systems have been rare in the literature. 1D radiative–convective modelling of WD 0137−349B performed in Casewell et al. (2015) suggests that the photometry of the BD is best fit with a full circulation efficiency, and without the presence of strong optical wavelength opacity sources such as TiO and VO molecules. UV photochemical effects such as H_2 fluorescence and H_3^+ formation and emission were also examined as candidates for boosting the K_s-band emission flux. Similar modelling and conclusions were found for the SDSS J141126.20+200911.1 system in Casewell et al. (2018b). Longstaff et al. (2017) adapted a DRIFT-PHOENIX (Witte, Helling & Hauschildt 2009; Witte et al. 2011) ($T_{\rm eff} = 2000$ K, $\log g = 5$, [M/H] = 0) atmospheric profile with a hot chromospheric region to examine the thermal dissociation and ionization profiles of the species detected in their observations.

Hernández Santisteban et al. (2016) used an energy balance model with a simplified redistribution efficiency parameter for the WD–BD interacting binary system SDSS J143317.78+101123.3. Their best-fitting parameters suggest poor day/night energy transport efficiency.

2.1 Dynamical expectations from HJ studies

WD–BD short-period binaries inhabit a unique parameter regime, namely moderate to strong irradiation with a fast rotation rate. Table 1 shows our adopted WD 0137−349 system parameters.

Komacek & Showman (2016), Komacek, Showman & Tan (2017), and Komacek & Tan (2018) examine the effect of increasing irradiation on HJ atmospheric circulation show that with increasing effective temperature, the radiative time-scales become shorter, resulting in a higher day–night temperature contrast and inefficient day–night energy transport. Several studies have examined the effects of rotation rate on the dynamical regime of the atmosphere, with and without the assumption of tidal locking (e.g. Showman et al. 2008, 2009; Kataria et al. 2013; Rauscher & Kempton 2014; Showman, Lewis & Fortney 2015; Komacek et al. 2017; Penn & Vallis 2017). In the short orbital period and forcing regime of WD 0137−349B, the above studies suggest the formation of a Matsuno–Gill flow pattern (Matsuno 1966; Gill 1980) commonly seen in HJ simulations, along with a multiple banded jet structure due to the higher rotation rate.

Tan & Komacek (2019) examined the effects of both increasing irradiation and rotation rates in the context of modelling ultra-HJ atmospheres, finding similar conclusions to the studies above without H_2 dissociation and recombination. Including the cooling/heating effects of H_2 dissociation/recombination reduced the day–night temperature contrasts in their simulations compared to no H_2 dissociation/recombination.

An estimate for the radiative time-scale, $\tau_{\rm rad}$ (s), is given by (Showman & Guillot 2002)

$$\tau_{\rm rad} \sim \frac{p}{g}\frac{c_p}{4\sigma T^3}, \tag{1}$$

where c_p (J kg^{-1} K^{-1}) is the heat capacity at constant pressure. For WD 0137−349B, taking $p = 10$ bar, $g = 1000$ m s^{-2}, $c_p = 14\,308$ J kg^{-1} K^{-1}, and $T = T_{\rm eq} = 1995$ K gives $\tau_{\rm rad} \sim 7945$ s. This value is small compared to typical values at this pressure ($\tau_{\rm rad} \sim 10^6$) in HJ atmospheres (e.g. Showman et al. 2008), and is more typical of mbar pressures in HJ atmospheres. This suggests the high gravity has a major effect reducing the heat redistribution efficiency by lowering the radiative time-scales as a whole in the atmosphere.

We also examine derived atmospheric regime parameters similar to Kataria et al. (2016). The Rossby number, Ro, is given by

$$\mathrm{Ro} = \frac{U}{fL}, \tag{2}$$

where $f = 2\Omega\sin\phi$, U a characteristic horizontal velocity, which we follow Kataria et al. (2016) and approximate as the global rms velocity expression from Lewis et al. (2010) at the IR photospheric pressure (10 bar) yielding $U \approx 1000$ m s^{-1}. We calculate f at mid-latitude and assume $L = 1.1\,R_{\rm jup}$. We estimate the Rhines scale, L_β (m), from

$$L_\beta = \pi\sqrt{\frac{U}{\beta}}, \tag{3}$$

where $\beta = 2\Omega\cos\phi/R_{\rm p}$ is evaluated at the equator. The Rossby deformation radius, $L_{\rm D}$ (m), is estimated through

$$L_{\rm D} = \frac{NH}{f}, \tag{4}$$

where N is the Brunt–Väisälä frequency and f calculated at mid-latitude. Table 2 presents these values for WD 0137−349B along with a selection of other objects.

From these estimates, WD 0137−349B occupies a distinct dynamical regime. It is most like Jupiter with small Ro, $L_{\rm D}$, and L_β, but occupies a radiative regime more typical of HJs.

Table 2. Characteristic values and scales of WD 0137−349B compared to a selection of other planets. Values were sourced from Parmentier (2014). Kelt-9b, WASP-43b, and WASP-121b were estimated following the prescription in Parmentier (2014), where the characteristic velocity is taken as a range between 100 and 1000 m s^{-1}.

Object	R_p (R_J)	Ω (rad s^{-1})	g (m s^{-2})	T_{eq} (K)	H (km)	Ro (-)	L_D (R_p)	L_β (R_p)
WD 0137−349B	1.1[a]	9.155×10^{-4}	1086[a]	1995	6.64	≈0.01	≈0.01	≈0.26
Jupiter	1.0	1.4×10^{-4}	23.1	124	20	0.02	0.03	0.1
HD 209458b	1.36	2.1×10^{-5}	10.2	1450	520	0.04–1.0	0.4	0.5–3
Kelt-9b	1.89	4.91×10^{-5}	20.0	4051	734	0.01–0.4	0.2	0.3–2
WASP-43b	1.04	8.94×10^{-5}	47.4	1441	110	0.01–0.4	0.1	0.3–2
WASP-121b	1.87	5.70×10^{-5}	8.4	2358	1010	0.01–0.4	0.1	0.3–2

[a]Denotes an estimated value.

Table 3. Adopted GCM simulation parameters. Adapted for the WD 0137−349 system from the Heng, Frierson & Phillipps (2011) HJ simulation parameters.

Symbol	Value	Unit	Description
F_0	3.59×10^6	W m^{-2}	Stellar irradiation constant
A_B	0.1	–	Bond albedo
T_{int}	500	K	Internal temperature
P_0	220	bar	Reference surface pressure
τ_{S_0}	15.68	–	Shortwave surface optical depth
$\tau_{L_{eq}}$	22.0	–	Longwave surface optical depth
n_S	1	–	Shortwave power-law index
n_L	1	–	Longwave power-law index
c_P	14308.4	J K^{-1} kg^{-1}	Specific heat capacity
R	4593	J K^{-1} kg^{-1}	Ideal gas constant
κ	0.321	J K^{-1} kg^{-1}	Adiabatic coefficient
g_{BD}	1000	m s^{-2}	Acceleration from gravity
R_{BD}	7.86×10^4	km	Radius of brown dwarf
Ω_{BD}	9.155×10^{-4}	rad s^{-1}	Rotation rate of brown dwarf
Δt	20	s	Simulation time step
T_{init}	1824	K	Initial isothermal temperature
N_v	50	–	Vertical resolution
d_2	0.02	–	Div. dampening coefficient

3 GCM MODELLING USING EXO-FMS

We use the three-dimensional, finite-volume Flexible Modelling System (FMS) GCM model (Lin 2004), previously used to model terrestrial exoplanet atmospheres (Exo-FMS; Pierrehumbert & Ding 2016; Hammond & Pierrehumbert 2017). We update Exo-FMS to use a cubed-sphere grid (e.g. Showman et al. 2009) with a resolution of C48 (≈192 longitude × 96 latitude). This set-up has recently been benchmarked for HJ-like conditions (Lee et al., in preparation).

Exo-FMS evolves the primitive equations of meteorology (e.g. Mayne et al. 2014; Komacek & Showman 2016) with a convective adjustment scheme. We adopt a similar GCM set-up to the dual-band HJ simulations performed in Heng et al. (2011), with the appropriate conditions for WD 0137−349B. An assumed radius of 1.1 Jupiter radii ($R_J = 7.1492 \times 10^4$ km), surface gravity of $g_{BD} = 1000$ m s^{-2}, and Bond albedo of $A_B = 0.1$ is taken for the BD. We use a 50 vertical layer set-up that is set using a hybrid sigma coordinate grid, approximately log spaced in pressure between 220 and 10^{-4} bar. A summary of the input parameters used for the GCM model is given in Table 3.

The model is run for a total of 3500 simulated Earth days, equivalent to ≈43 448 orbital periods. The outputs presented here are an average of the last 500 d of simulation. In Fig. 1, we show the global rms velocity at each pressure level during the 3500 d simulation.

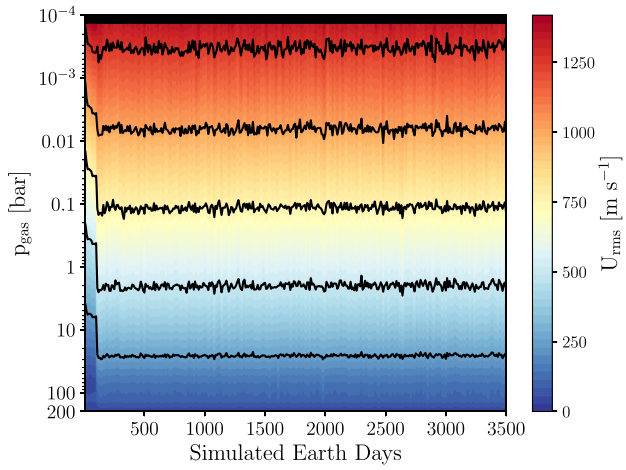

Figure 1. Global rms velocity as function of pressure with simulated time. The jump at 100 d corresponds to the turning off of a stronger Rayleigh drag used to stabilize the simulation during spin-up.

3.1 Radiative transfer

In order to avoid the difficulties associated with modelling UV radiative heating and associated photochemical heating, for radiative transfer inside the GCM we use a double-grey scheme. We assume the IR and optical grey opacity values from Guillot (2010) given by $\kappa_{IR} = 10^{-2}$ cm^2 g^{-1} and $\kappa_V = 6 \times 10^{-3} \sqrt{(T_{irr}/2000)} = 7.134 \times 10^{-3}$ cm^2 g^{-1}. Because of the higher surface gravity of the BD ($g_{BD} \sim 1000$ m s^{-2}) compared to typical HJs ($g_{HJ} \sim 10$ m s^{-2}), the atmospheric vertical extension is much reduced compared to a HJ. This results in the IR optical depth at the reference pressure of our model (220 bar) of $\tau_{L_{eq}} = 22$ and visual optical depth of $\tau_{S_0} = 15.68$, substantially lower than typical HJ simulations (e.g. Heng et al. 2011; Rauscher & Menou 2012).

With the absence of a deep optically thick region, this suggests the dayside to be mostly dominated by the irradiation from the white dwarf. The radiative time-scale on the dayside is estimated to be short for the WD 0137−349B parameters (e.g. Showman et al. 2008), suggesting the dayside profiles are expected to be near radiative equilibrium. Since day–night energy redistribution by flows is suggested to be weak for such systems (Section 2.1), nightside profiles are expected to be colder and primarily controlled by the internal flux.

To estimate the internal flux, we assume WD 0137−349B follows the HJ population trends and use the expression of Thorngren, Gao & Fortney (2019). This yields a value of $T_{int} = 665$ K, we therefore

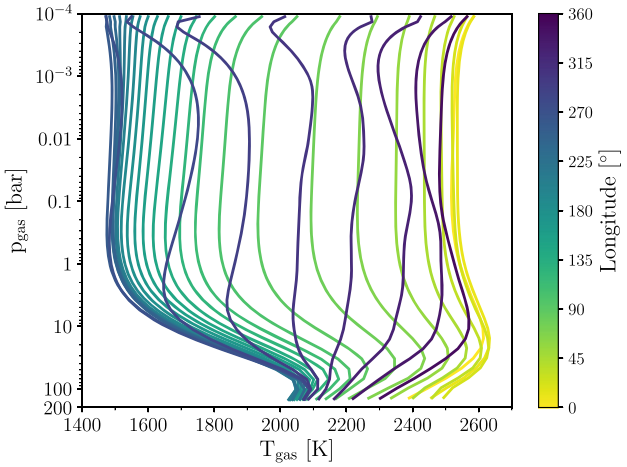

Figure 2. One-dimensional temperature–pressure profiles at the equatorial region of the GCM output. The colour bar shows the longitude of the profile.

adopt a T_{int} of 500 K for this study as a more tractable value in our GCM model.

3.2 Numerical stability

To aid numerical stability of the GCM we apply the 'basal' drag formulation of Liu & Showman (2013) in the lower atmospheric regions, commonly used in (ultra)HJ GCM studies (e.g. Komacek & Showman 2016; Tan & Komacek 2019; Carone et al. 2020) motivated as a mimic to magnetic drag forces. This takes the form of a pressure-dependent linear drag, $F_{dr}(p)$ (m s^{-2}), in the horizontal momentum equation (Komacek & Showman 2016; Carone et al. 2020):

$$F_{dr}(p) = -\frac{\boldsymbol{v}}{\tau_{dr}(p)}, \tag{5}$$

where $\boldsymbol{v}$ (m s^{-1}) is the local velocity vector and $\tau_{dr}(p)$ (s) the pressure-dependent drag time-scale. $\tau_{dr}(p)$ is given as a linear function of pressure between a prescribed top and bottom pressure level ($p_{dr,\,t}$ and $p_{dr,\,b}$, respectively) where the drag force is present,

$$\tau_{dr}(p) = \tau_{dr,b}\frac{(p - p_{dr,t})}{(p_{dr,b} - p_{dr,t})}, \tag{6}$$

where $\tau_{dr,\,b}$ (s) is the drag time-scale at the simulation lower boundary (here taken as 1 Earth day). We take $p_{dr,\,b}$ to be the lower boundary pressure (220 bar) and $p_{dr,\,t} = 10$ bar.

4 ATMOSPHERIC STRUCTURE OF WD 0137−349B

In this section, we present the thermal and dynamical structures of the WD 0137−349B GCM simulation. Fig. 2 shows the 1D temperature–pressure profiles at the equatorial region of the BD. Dayside profiles are close to isothermal down to a pressure of ≈10 bar, where the atmosphere becomes optically thick in the optical band. This suggests the atmosphere to be near radiative equilibrium in most parts of the dayside atmosphere.

Fig. 3 shows latitude–longitude (lat–lon) maps of the temperature and velocity vector fields at pressure levels 10^{-3}, 0.01, 0.1, 1, 10, and 100 bar. These maps show that the main redistribution of energy from the dayside to the nightside comes from the strong equatorial confined jet. There is also significant westward shifting of hotspots from the dayside at latitudes of ±20° from counter-rotating jets, and a slight shifting eastward at ∼±30° latitude.

Fig. 4 presents the zonal mean temperature, zonal velocity, vertical velocity, and mass stream function. The zonal mean temperature and zonal velocity plots show that efficient day–night energy transport is present at the equatorial regions of the model. Regions at high latitudes, outside the main jet structures remain colder on average. The zonal mean velocity plot suggests that global scale jets and counter-rotating jets are present. However, the velocity vectors in the temperature map plots (Fig. 3) suggest a more complex atmospheric wave structure, with a mixture of flows going with and against the rotation. We briefly discuss these dynamical features in Section 6.

The zonal mean vertical velocity plot suggests global scale upwelling and downwelling occurring inside the BD atmosphere. However, in Fig. 5, we show the lat–lon pressure level maps of the vertical velocity. These plots show that the downwelling is localized near the 270° longitude terminator and at the equator and ±20° latitudes, while the majority of the upwelling is located on the dayside of the BD. The zonal mass stream function plot along with the vertical velocity plots in Fig. 5 suggests multiple overturning structures at the 270° longitude terminator.

4.1 OLR and atmospheric variability

Fig. 6 (left) presents the columnwise top of atmosphere (TOA) outgoing longwave radiative (OLR) flux of the averaged output. The pattern corresponds well to the temperature structure from 1 to 10 bar (Fig. 3), the expected pressure levels where the longwave radiation becomes optically thin.

To examine the variability in our model, we calculate the latitudinally averaged OLR flux, $\langle F_{OLR}\rangle$ (W m^{-2}), given by (e.g. Heng et al. 2011)

$$\langle F_{OLR}\rangle = \frac{1}{\pi}\int_{-\pi/2}^{\pi/2} F_{OLR}\cos^2\Phi\,\mathrm{d}\Phi, \tag{7}$$

where F_{OLR} (W m^{-2}) is the columnwise OLR flux from the GCM model. In the right-hand panel of Fig. 6, we present the averaged flux from equation (7) as a function of longitude for every 10 d for the final 500 d of simulation. The OLR variation is $\lesssim 0.25 \times 10^6$ W m^{-2} on the dayside phases of the BD, while nightside phases remain relatively constant with time. A slight westward shift (≈5°) in the maximum OLR is also present as shown by the vertical dotted line.

5 POST-PROCESSING AND COMPARISON TO OBSERVATIONS

In this section, we produce synthetic emission spectra and phase curves from the GCM results to compare directly to the available observational data. We apply the hybrid ray tracing and 3D Monte Carlo radiative transfer model CMCRT (Lee et al. 2017) in correlated k mode (Lee et al. 2019) to calculate the output emission spectra of the GCM. Because of the strong day–night temperature contrast, we apply the composite emission biasing of Baes et al. (2016) with a ξ_{em} bias coefficient of 0.99. We also develop a biasing scheme for sampling the k-coefficients in emission, detailed in Appendix A, based on the Baes et al. (2016) methodology. To avoid spurious noise from the inverted temperature profiles near the uppermost boundary layers (e.g. Fig. 2), the temperature of the top two layers is assumed to be equal to the third most upper layer.

The volume mixing ratio of molecular and elemental species is calculated assuming chemical equilibrium (CE) using the GGCHEM

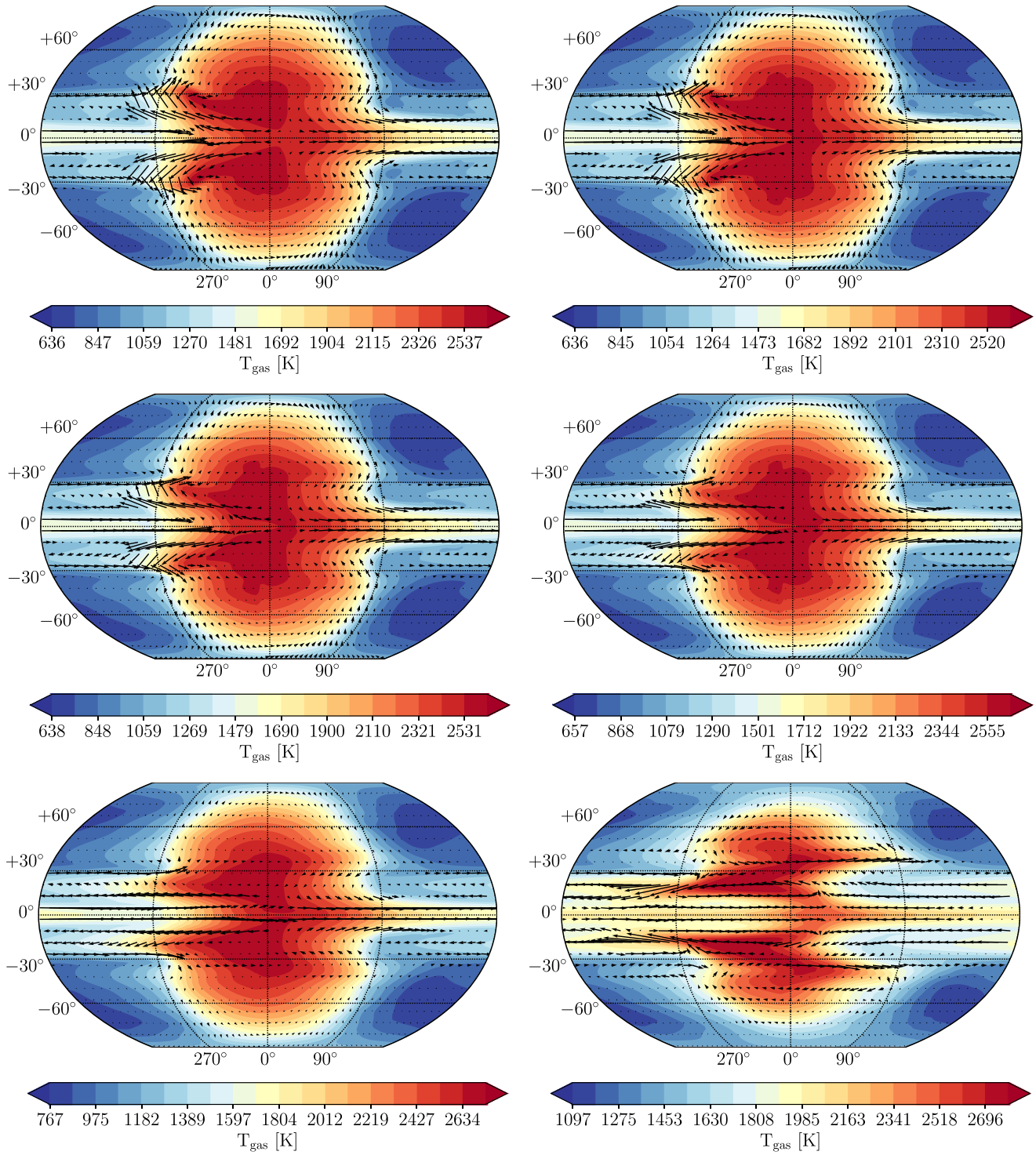

Figure 3. Atmospheric gas temperatures, $T_{\rm gas}$ (K), latitude–longitude (lat–lon) maps at approximately 10^{-3} and 0.01 bar (top row), 0.1 and 1 bar (middle row), and 10 and 100 bar (bottom row) gas pressures. The vectors show the direction and relative magnitude of the wind speed. Note the scale is different between each plot.

code (Woitke et al. 2018) at the solar elemental ratios from Asplund et al. (2009). We include the calculation of thermally ionized species in the CE calculation to more accurately capture the chemical structure of the hotter ($T_{\rm gas} > 2000$ K) atmospheric regions.

A key difference between typical HJ phase curve modelling and this system is the low inclination of WD 0137−349B (∼35°), resulting in different higher latitude fractions of the BD dayside and nightside regions in the observational line of sight at each phase. CMCRT takes this into account by calculating the viewing angles as

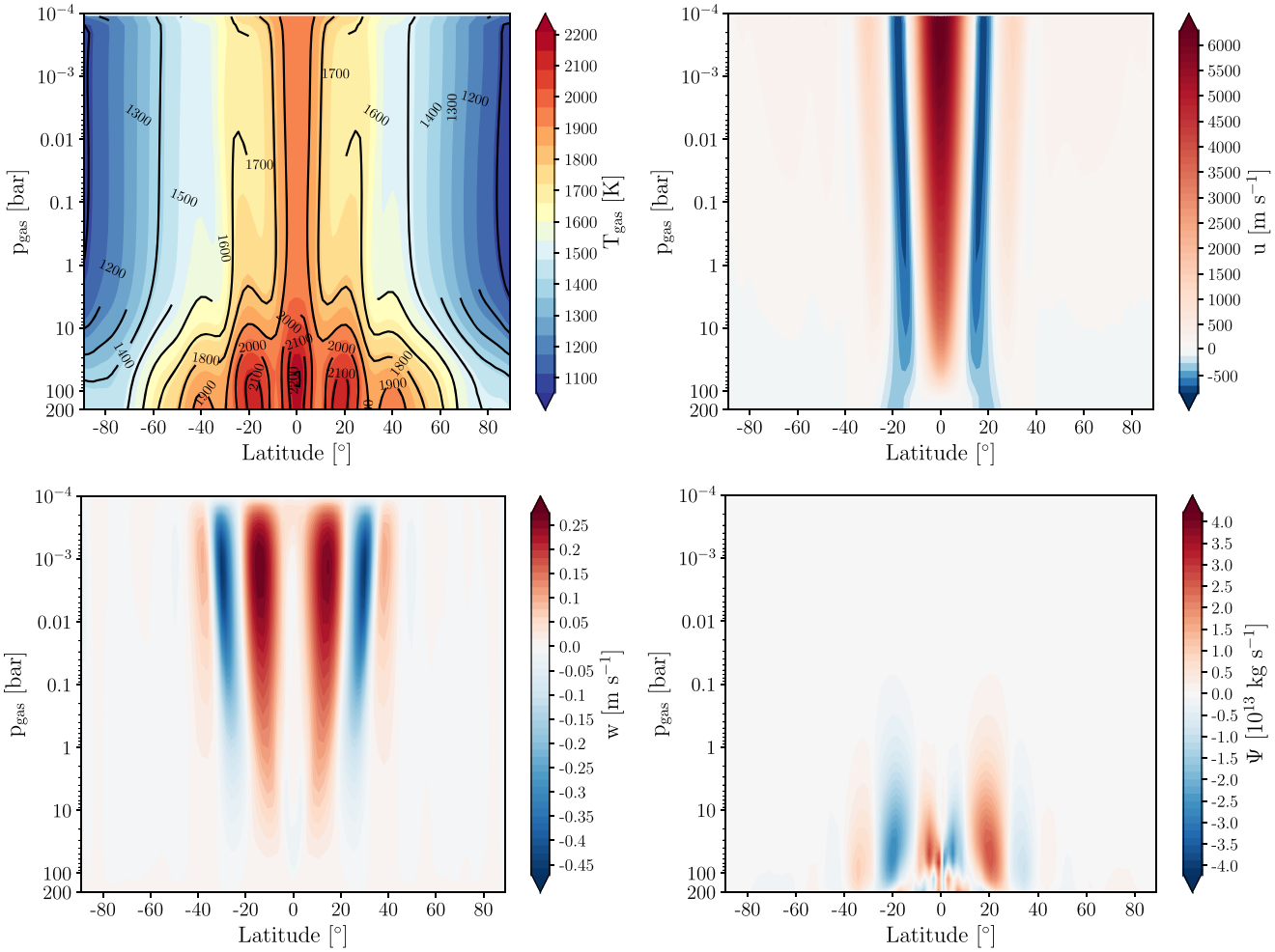

Figure 4. Zonal mean of the gas temperature [$T_{\rm gas}$ (K), top left], zonal velocity [u (m s^{-1}), top right], vertical velocity [w (m s^{-1}), bottom left], and mass stream function [Ψ (kg s^{-1}), bottom right].

a function of phase for a 35° system inclination (i.e. viewing the planet at latitude of +55°). To produce combined WD+BD fluxes we use the same WD model as in Casewell et al. (2015), originally produced from the TLUSTY and SYNSPEC models (Hubeny 1988; Hubeny & Lanz 1995). The WD fluxes were convolved with the *H*, *J*, $K_{\rm s}$, and *Spitzer* filter profiles to calculate the WD flux in each band.

5.1 Input opacities

Our molecular *k*-coefficients are calculated from the ExoMol data base (Tennyson et al. 2016) line lists with H_2 pressure broadening at a resolution of R1000 between 0.3 and 300 μm. For Na and K we take the line list from the National Institute of Standards and Technology (NIST) data base (Kramida, Ralchenko & Reader 2013) and broadening profile based on Allard, Kielkopf & Allard (2007). Table 4 contains all opacity sources used in the CMCRT simulation and their associated references. The opacity of each GCM cell is calculated by interpolating from the table of *k*-coefficients of each species and combined using the random overlap method (e.g. Lacis & Oinas 1991; Amundsen et al. 2017).

5.2 Emission spectra

Fig. 7 (left-hand panel) shows the emission spectrum of the model WD and the post-processed GCM output at 0 and 0.5 phase. The observational bandpasses of the instruments used in Casewell et al. (2015) are also plotted. Each band is sensitive to the opacity features of different molecules considered in this study:

(i) *V* band: Na;
(ii) *R* band: Na & K;
(iii) *I* band: K;
(iv) *J* band: H_2O, CH_4, NH_3;
(v) *H* band: H_2O, NH_3;
(vi) $K_{\rm s}$ band: CH_4, NH_3;
(vii) *Spitzer* 3.6: CH_4;
(viii) *Spitzer* 4.5: CO, CO_2;
(ix) *Spitzer* 5.8: H_2O;
(x) *Spitzer* 8.0: H_2O, CH_4, NH_3.

Any absorption features in the model emission spectra or modulations seen in the phase curves are therefore a convolution of the differences in the photospheric temperatures as a function of phase and also any change in the chemical composition between hemispheres.

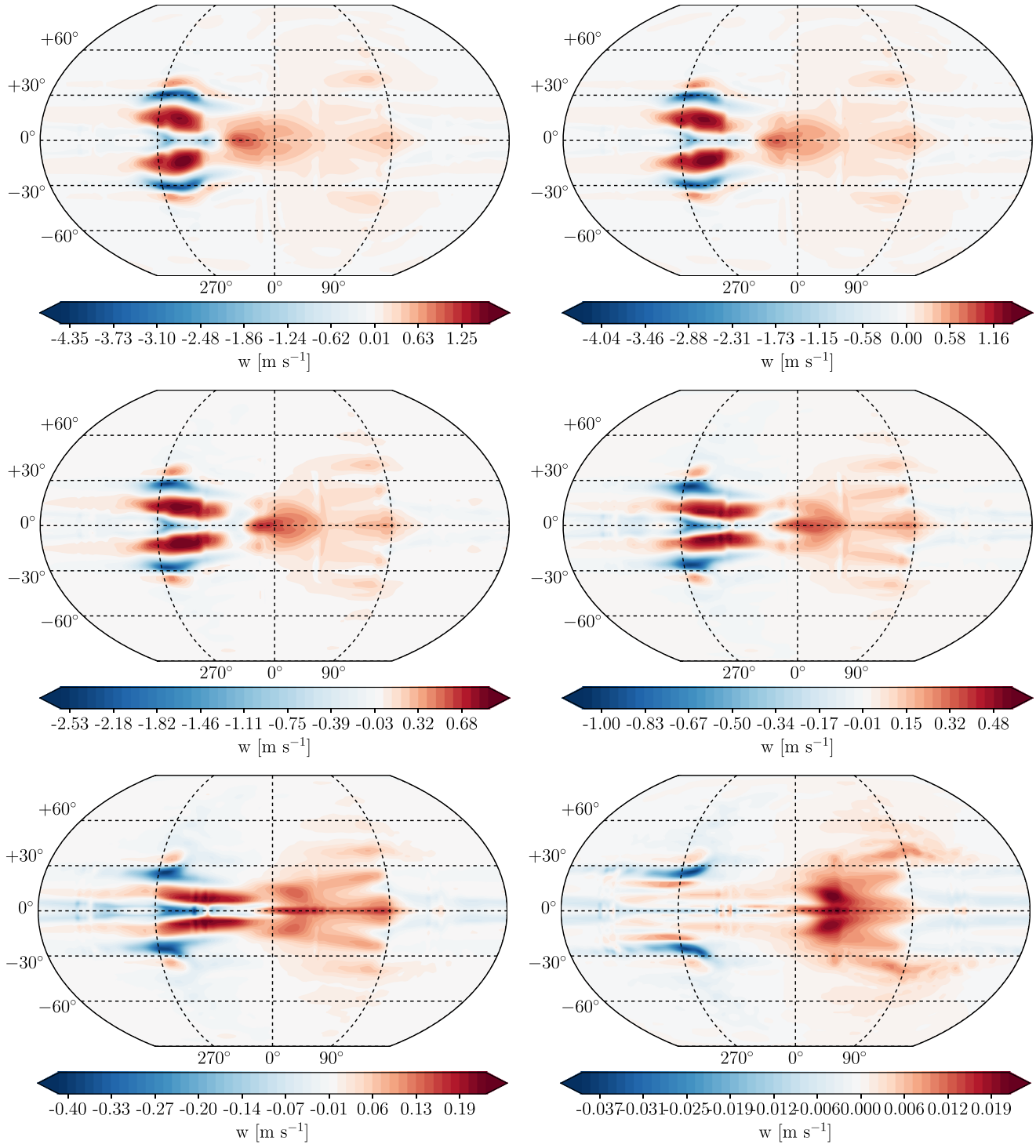

Figure 5. Atmospheric vertical velocity, w (m s^{-1}), latitude–longitude (lat–lon) maps at approximately 10^{-3} and 0.01 bar (top row), 0.1 and 1 bar (middle row), 10 and 100 bar (bottom row) gas pressures. Note the scale is different between each plot.

We reproduce the start of the near-IR excess at ≈1.95 μm observed at the nightside phase of the BD in Burleigh et al. (2006) (Fig. 7, right-hand plot), suggesting that the fraction of the dayside and nightside emission of the BD at an orbital inclination of 35° is a reasonable approximation, rather than the expected $T_{\rm eq} \sim 2000$ K emitted flux at a 90° inclination.

Our model is unable to reproduce the Na and K emission features reported on the dayside of the BD by Longstaff et al. (2017). This is due to a lack of an upper atmosphere temperature inversion present in the GCM thermal structures. We suggest possible mechanisms to produce such an inversion in Section 6.

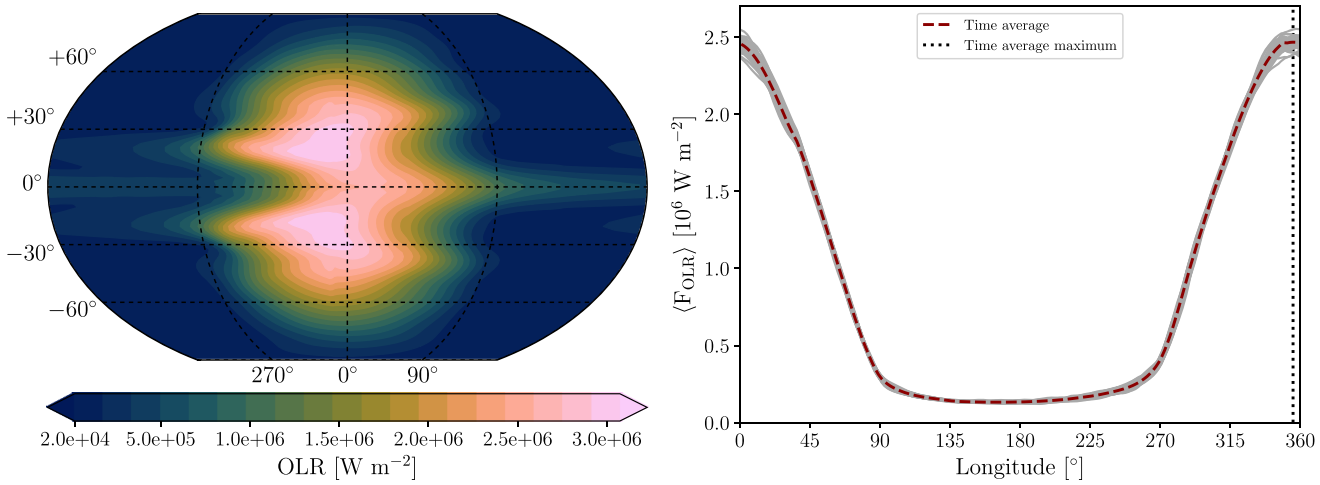

Figure 6. Left: map of outgoing longwave radiation (OLR) flux (W m^{-2}) from the GCM model. Right: latitudinally averaged OLR flux, $\langle F_{\rm OLR}\rangle$ (equation 7), as a function of longitude. The red dashed line shows the time-averaged value, the grey lines show output every 10 d for the final 500 d of simulation, and the vertical dotted line shows the longitude of the time-averaged maximum flux.

Table 4. Opacity sources and references used in the CMCRT post-processing of the GCM model output.

Opacity source	Reference
Line	
Na	Kramida et al. (2013)
K	Kramida et al. (2013)
H_2O	Polyansky et al. (2018)
CH_4	Yurchenko et al. (2017)
NH_3	Yurchenko, Barber & Tennyson (2011)
CO	Li et al. (2015)
CO_2	Rothman et al. (2010)
Collision-induced absorption	
H_2–H_2	Baudino et al. (2017)
H_2–He	Baudino et al. (2017)
Rayleigh scattering	
H_2	Irwin (2009)
He	Irwin (2009)

5.3 Phase curve comparisons

In this section, we produce synthetic phase curves of our model for the bands used in the Casewell et al. (2015) observational campaign. We focus on the IR photometric bands *J*, *H*, K_s, and *Spitzer* 3.6, 4.5, 5.8, and 8.0 μm bands. For a fair comparison to the Casewell et al. (2015) data, the WD model flux in each band is added to each synthetic phase curve. From Fig. 7, during nightside phases significant flux in the IR, *J*, *H*, K_s, and *Spitzer* bands is contributed by the WD. Including this IR emission from the WD is required to 'flatten out' the phase curves near 0.5 phase and better reproduces the observed phase curve shapes.

Our model generally overpredicts the flux in each IR bandpass (left-hand plot of Figs 8 and 9) by factors of ≈1–3. We scale each model phase curve by the relative difference between the average flux of the model and observations to compare the shape of the phase curve (right-hand plot of Figs 8 and 9). Table 5 presents the required scaling factors for each band. The scaled model phase curves match the observed phase curves shapes well, suggesting the peak to trough amplitudes are reasonably approximated in the GCM simulation. The *H*, K_s, and *Spitzer* 3.6 μm bands would require some additional flattening to better fit the observed shape. This suggests that either the day–night contrast is too large in these bands (i.e. the day–night heat transport is too weakly modelled here), or the chemical abundances composition may be different to those calculated here, potentially through non-equilibrium effects. No discernible phase curve offset is produced in the model output, with a highly symmetric profile, typical of current WD–BD phase curve data (e.g. Parsons et al. 2017; Casewell et al. 2018a). This is due to the low inclination angle of 35° that does not have a large flux contribution from the westward shifted patters closer to the equator (Fig. 6).

6 DISCUSSION

In this section, we discuss our results in context and suggest additional considerations for future modelling efforts.

6.1 Atmospheric structure and dynamics

The main dynamical feature of the BD simulations is the significant narrower meridional extent of the equatorial super-rotating jet compared to typical HJ simulations (e.g. see review by Heng & Showman 2015). Because of the fast rotation, high gravity (small scale height) of the BD, the Rossby deformation radius is significantly smaller compared to typical HJ systems. This leads to the expected Matsuno–Gill flow pattern being compressed at ∼±30° latitude.

At higher latitudes, winds are much weaker than that at low latitudes, together with the fast rotation (large Coriolis force) implying a geostrophic circulation regime there. As a result, wind vectors follow closely parallel to isotherms. The horizontal thermal structure poleward of ±45° latitude closely resembles an equilibrium structure. This is consistent with the analytic wave solution of Showman & Polvani (2011) assuming no frictional drag (which is effectively assuming geostrophy). Finally, hourly outputs of our simulation also exhibit small-scale instability mostly around mid-latitudinal and counter-rotating flow regions, presumably caused by baroclinic instability. These features are probably responsible for the dayside variability in the OLR (Section 4.1). Similar instabilities were examined by Showman et al. (2015), Fromang, Leconte &

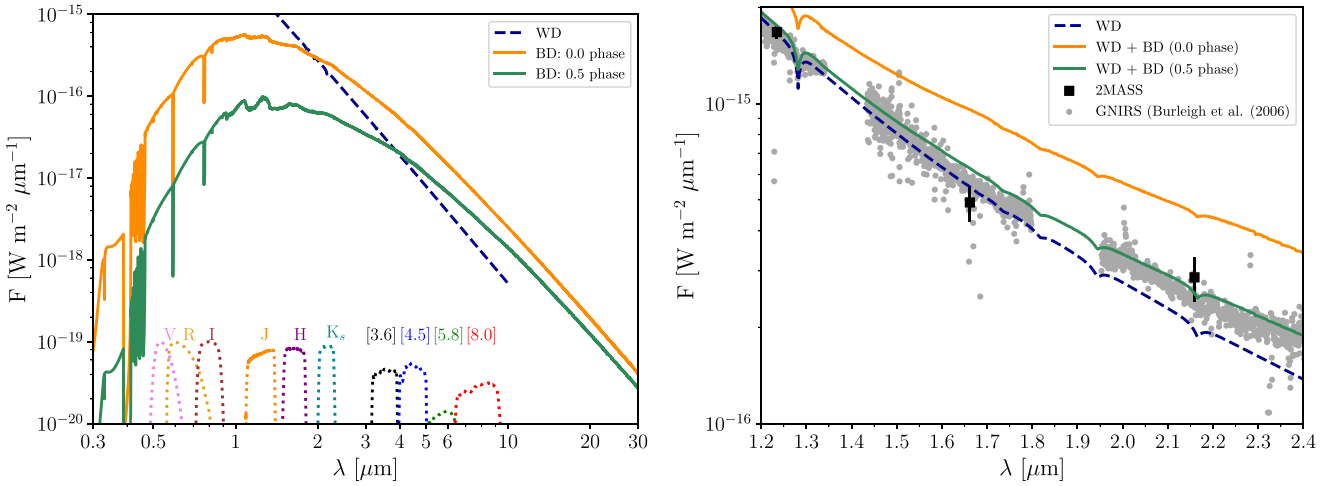

Figure 7. Left: post-processed emission spectra of the BD model at 0 (orange) and 0.5 (green) phases. Right: model emission spectra between 1.2 and 2.4 μm with archival Two Micron All-Sky Survey (2MASS) photometry data (black points) and the Gemini Near-Infrared Spectrograph (GNIRS) spectra from Burleigh et al. (2006) (grey points). The modelled WD flux is the dashed blue line. The bandpasses used in Casewell et al. (2015) are plotted as dotted lines near the *x*-axis.

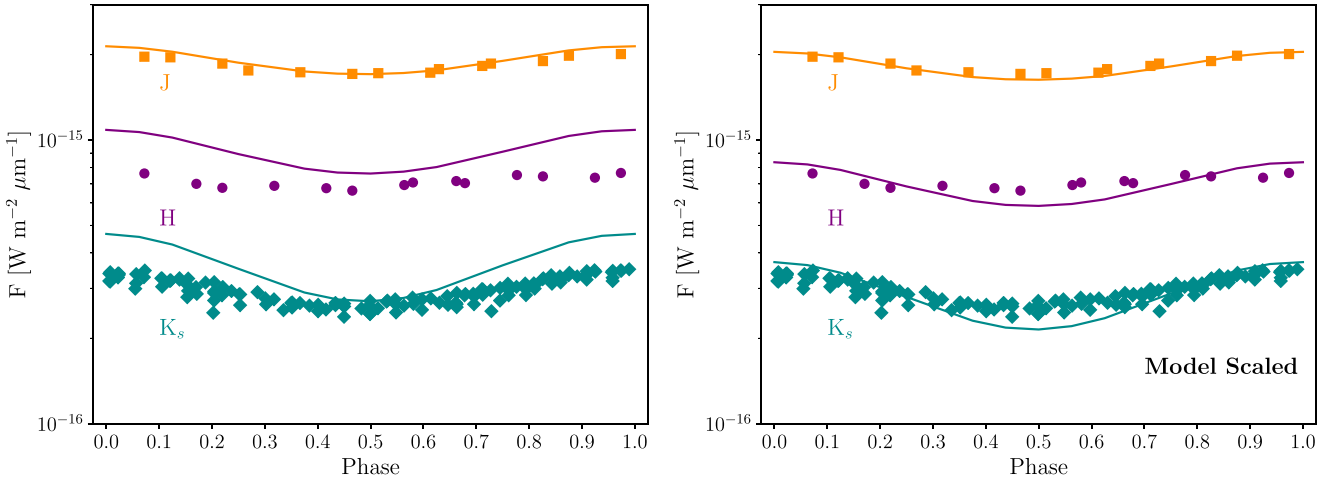

Figure 8. *J* (orange), *H* (purple), and K_s (cyan) band phase curves from Casewell et al. (2015) (points) and post-processed GCM model fluxes (lines). The left-hand plot shows the fiducial model fluxes, while the right-hand plot shows the model fluxes normalized to the average observed flux in each band, given by the relative factors in Table 5. Errors in the observational data are on the order of the point size.

Heng (2016), and Menou (2020) that focused on meandering of the equatorial jet in HJ simulations.

Carone, Keppens & Decin (2015), Penn & Vallis (2017, 2018), and Carone et al. (2020) investigate mechanisms for possible westward offsets in phase curves for tidally locked, fast rotating planets as the dynamics becomes more rotationally dominated. As a highly rotational-dominated regime, our simulations exhibit a similar mechanism to the above studies. However, the Rossby wave gyres in our model are compressed closer to the equator, which also leads to a westward hotspot shift as viewed at equatorial latitudes.

In a parallel study, Tan & Showman (2020) explored atmospheric circulation of tidally locked WD–BD systems with decreasing rotation period down to 2.5 h. The atmospheric circulation of the most rapidly rotating case is qualitatively similar to the results presented here, showing a narrowing equatorial super-rotating jet, nearly geostrophic flows at mid–high latitudes and larger day–night temperature difference than those of typical HJ simulations. Although using different GCM and radiative forcing set-up, the agreement between two studies is quite encouraging. Carone et al. (2020), Tan & Showman (2020), and this study also show agreement on the formation of a westward hotspot shift as a consequence of the fast rotation rate.

Future studies on similar objects should consider increasing the resolution of the GCM simulation in order to capture the smaller scale features. Tests performed in Showman et al. (2015) (however for slower rotation rates than modelled here) suggest a resolution of C48 is sufficient to capture the larger scale dynamical features.

We note that Carone et al. (2020) suggest that when simulating faster rotating HJ objects ($P_{\rm orb} \lesssim 1.5$ d) then a deeper lower boundary (e.g. $P_0 = 700$ bar) is used. In this study, we chose a bottom boundary of 220 bar in order to directly compare to typical HJ GCM set-ups. Although we do not capture potentially important deeper atmospheric motions, our set-up captures the important photospheric pressures where most of the observable flux emerges

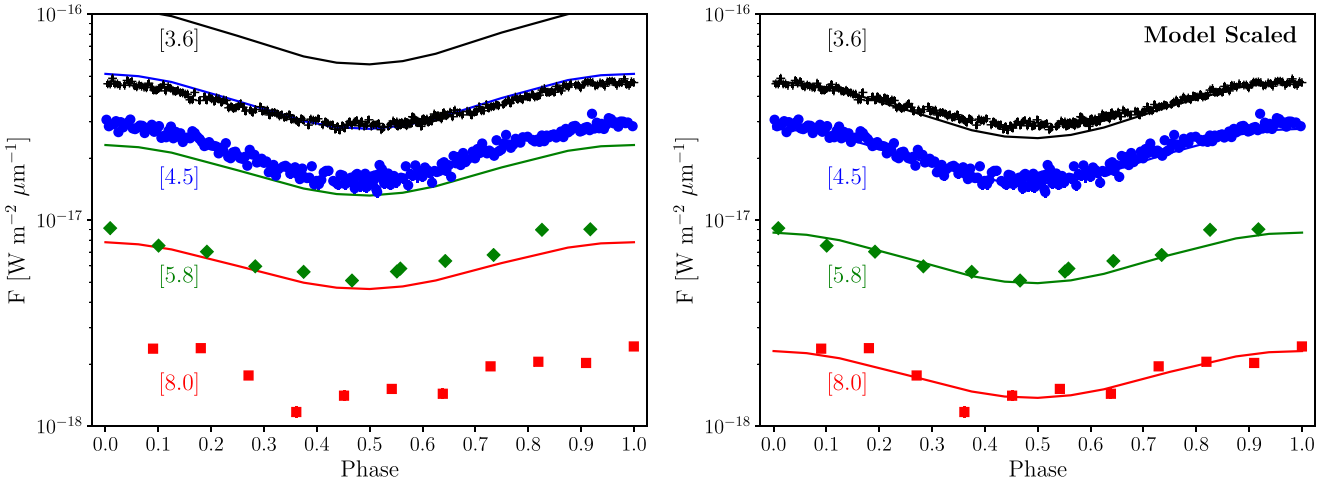

Figure 9. [3.6] (black), [4.5] (blue), [5.8] (green), and [8.0] (red) μm *Spitzer* band phase curves from Casewell et al. (2015) (points) and post-processed GCM model fluxes (lines). The left-hand plot shows the fiducial model fluxes, while the right-hand plot shows the model fluxes normalized to the average observed flux in each band, given by the relative factors in Table 5. Errors in the observational data are on the order of the point size.

Table 5. Average relative phase curve flux shift required for the model in each IR band to match observed fluxes.

Band	Av. rel. shift
J	1.047
H	1.300
K_s	1.257
[3.6]	2.282
[4.5]	1.848
[5.8]	2.662
[8.0]	3.376

from. Future GCM modelling efforts for short-period WD–BD should strongly consider simulating to a greater atmospheric pressure in order to capture any deeper dynamical phenomena, but also to more accurately simulate the radiative transfer in the deeper optically thick regions, not probed in the current study. However, a surface boundary of $P_0 = 1000$ bar would have an IR surface optical depth of $\tau_{L_{eq}} \approx 100$ for our simulation, still an order of magnitude below typical HJ values (e.g. Heng et al. 2011; Rauscher & Menou 2012). At these high pressures H_2–H_2 and H_2–He continuum opacity is an important IR opacity source, and so a power-law dependence on $\tau_{L_{eq}}$ (e.g. Heng et al. 2011; Rauscher & Menou 2012) may be more appropriate to include for a double-grey RT schemes.

6.2 Vertical mixing and non-equilibrium chemistry

Recent observations of the shorter period HJ WASP-43b (Chubb et al. 2020) and cool BDs (Miles et al. 2020) suggest non-equilibrium chemistry is an important consideration that shapes the spectrum of objects in a similar regime to WD 0137−349B. The weak vertical velocities and overturning seen in the GCM model at low–mid latitudes suggest that the upper atmosphere near the equatorial regions are slowly replenished from the deeper regions (Fig. 5). This may act to starve the supply of photochemically active species to the upper atmosphere. To examine this we utilize the 1D version of the chemical kinetic model VULCAN (Tsai et al. 2017). We calculate a K_{zz} (cm^2 s^{-1}) profile from the GCM results using the relation $K_{zz} = H w_z$ (e.g. Moses et al. 2011), where H is the scale height and w_z the rms vertical velocity across the quadrant. We average this value and the temperature–pressure profile across four quadrants, the dayside, nightside and East and West hemispheres. Our profiles are also extended to 10^{-8} bar to capture the important upper atmospheric regions for UV photochemistry. These are then used as input to the VULCAN model. We include photochemical and ion chemistry in the kinetic model. For the UV incident beam, we assume a hemispheric average zenith angle of 46° for the dayside profile and 74° for the terminator hemispheres.

Fig. 10 shows the results of the VULCAN model for each quadrant. It is clear that the overturning features on the western terminator (Fig. 5) produce the largest K_{zz} profiles, but mixing is overall weak at $K_{zz} \sim 10^6$ cm^2 s^{-1}. Our results show that significant photochemical-induced ionization of hydrogen and photochemical disassociation of molecules occur at the upper atmosphere ($p < 10^{-4}$ bar) for the dayside and terminator hemispheres. This region is dominated by a large fraction of neutral hydrogen, ionized hydrogen, and free electrons. The bottom right-hand panel of Fig. 10 compares the CH_4 chemical equilibrium and VULCAN results, suggesting that CH_4 is quenched from 10 to 100 bar on the east and west terminator regions, but in equilibrium on the dayside and nightside.

A 3D examination of the non-equilibrium chemistry could be considered for future studies, similar to recent GCM studies (e.g. Bordwell, Brown & Oishi 2018; Drummond et al. 2018, 2020; Mendonça et al. 2018; Steinrueck et al. 2019). Our results suggest consistent photochemical and ionization effects in the 3D model are also likely to be more important in the WD–BD cases than the HJ cases due to the high amount of UV flux the BD receives.

6.3 UV effects and heating in the upper atmosphere

Our modelled emission spectra were not able to reproduce the elemental emission features from the BD reported in Longstaff et al. (2017). This suggests that other mechanisms beyond that modelled in the GCM are required to produce an upper atmospheric temperature inversion. Absorption of UV photons and subsequent heating in the upper atmosphere is a possible candidate for producing a temperature inversion. The energy release by recombination of photochemical products occurring in the upper atmosphere could also be a source of significant heating. Longstaff et al. (2017) also suggest a chromospheric-like upper atmospheric region that

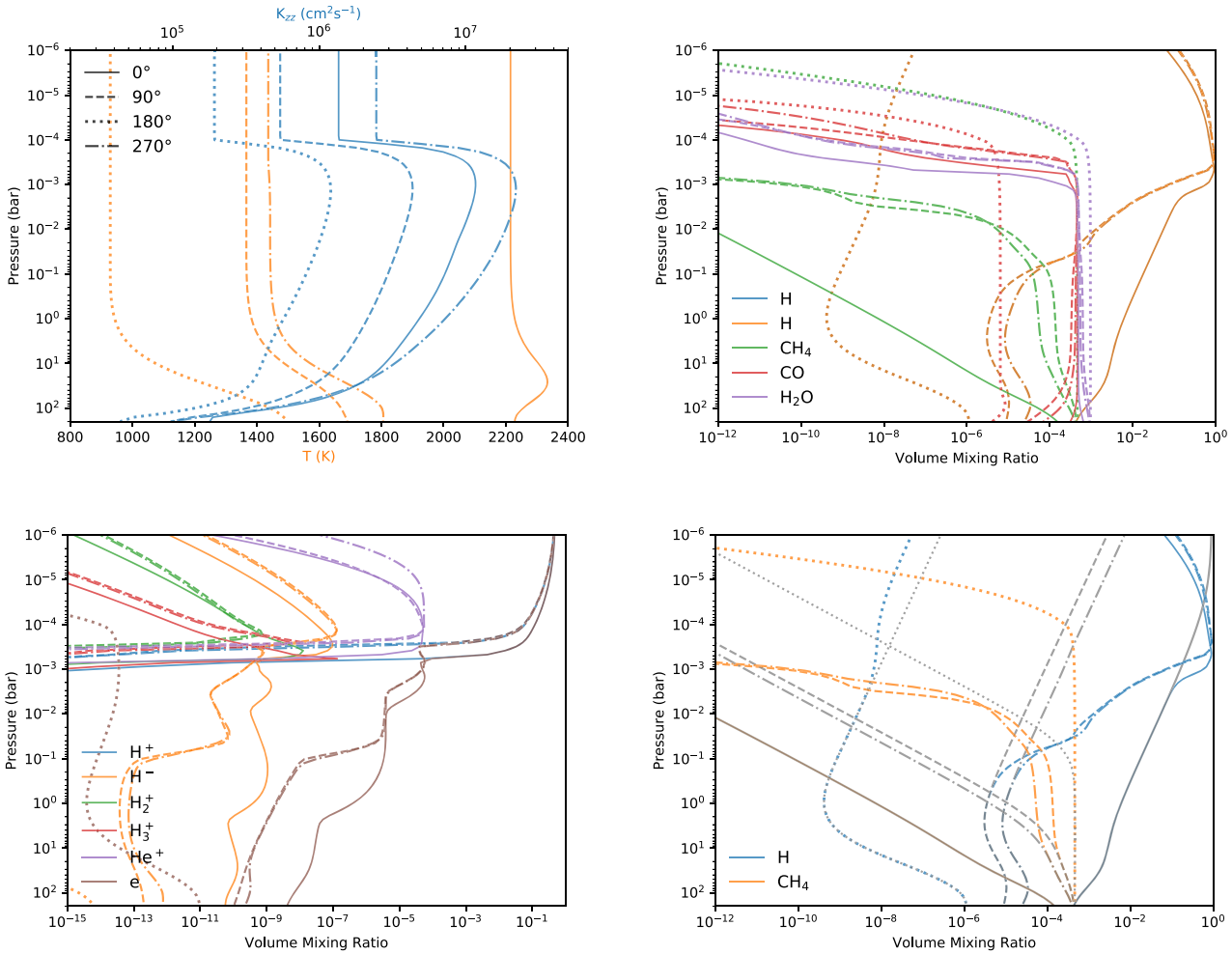

Figure 10. Top-left: *T–p* profiles with the derived K_{zz} from the GCM model for each quadrant. Top-right: VULCAN results for the neutral species. Bottom-left: VULCAN results for the ion species. Bottom-right: chemical equilibrium values (grey) compared to the VULCAN results for CH_4 and H. Solid, dashed, dotted, and dash–dotted lines correspond to the 0°, 90°, 180°, and 270° quadrants, respectively.

thermally disassociates molecules in addition to providing a strong temperature inversion region.

In this study, we have used the solar metallicity grey opacity parameters from Guillot (2010), tuned to reproduce an HD 209459b-like structure and irradiation by a main-sequence star at optical wavelengths. One of the major uncertainties for our modelling is the UV opacities for the BD atmosphere, and therefore the radiative heating from the primary UV irradiation by the WD. The Bond albedo is also a major uncertainty, should it be higher than that assumed here ($A_B = 0.1$), the atmosphere would be cooler than that modelled here.

We suggest a possible way to approximate the radiative heating from UV irradiation would be to split the shortwave scheme in the double-grey radiative transfer into a UV and visible component, each with a fraction of the total irradiative flux and separate 'Bond albedo'. The reference optical depth of the UV band can then be tuned to match the expected $\tau \sim 1$ at lower pressures (≈μbar to mbar) informed by photochemical kinetics modelling (e.g. Lavvas, Koskinen & Yelle 2014; Rimmer & Helling 2016) or 1D radiative–convective modelling (e.g. Lothringer, Barman & Koskinen 2018). Absorption of more shortwave energy in the upper atmosphere would also change the dynamical structure of the atmosphere, producing a shallower dynamical layer, potentially increasing the variability (and phase offset) of the photospheric regions compared to the current study. If the shortwave absorption becomes significant compared to the long-wave absorption, then the formation of a temperature inversion is also more favoured. The energy released from chemical recombination by photochemical products can also be estimated as a function of the UV band flux and the available photochemical products. A simplified, net photochemical species passive tracer scheme could also be included in the GCM to more accurately inform the replenishment rates of photochemical products to the upper atmosphere. A 3D chemical kinetics scheme was used in Yates et al. (2020) in a similar manner to model ozone production on Proxima Centauri b. The above schemes will be experimented with in our future modelling efforts.

6.4 Cloud formation and effect on OLR

The temperature structure results of the GCM model suggest that mineral cloud formation is likely to occur. Fig. 11 presents 1D *T–p* profiles from different locations from the GCM with the supersaturation curves of mineral materials from Lodders & Fe-

gley (2002), Visscher et al. (2006, 2010), Morley et al. (2012), and Wakeford et al. (2017) at solar elemental ratios. This plot suggests that significant cloud formation of multiple species is expected to occur on the nightside of the BD. The refractory elements and silicates are expected to form at deeper pressures than simulated here, however, mineral sulphide and salt species are likely to form in the nightside photospheric regions. We suggest the additional IR opacity provided by these clouds may act to warm the nightside regions by reducing the efficiency of atmospheric cooling.

Fig. 11 suggests refractory and silicate minerals can potentially form at higher latitudes on the dayside of the BD. This may have a more direct impact on the emission spectra, and hence phase curves, by providing additional opacity to the upper parts of the atmosphere that contribute the most flux to the synthetic observations. Much of the high latitude dayside regions are constantly in the line of sight at an orbital inclination of 35°, so this opacity may act to reduce the outgoing IR flux, generally overpredicted in our modelled phase curves (Figs 8 and 9). The weak vertical velocities and strong gravity of the BD suggest that only small, submicron cloud particles would be able to remain lofted in the photospheric regions.

We note the specific cloud structure will also depend on the internal temperature of the planet. Recent observations of WASP-121b by Sing et al. (2019) suggested Mg and Fe atoms present at high altitudes in the planet, potentially indicating a high internal temperature ($T_{\rm int} \sim 500$ K) that does not allow the condensation of refractory material at greater pressures. High-resolution spectra by Longstaff et al. (2017) of WD 0137−349B show that the strength of the refractory elements (e.g. Mg, Fe, and Si) decreases on nightside phases of the BD, indicating possible active condensation processes occurring in the atmosphere.

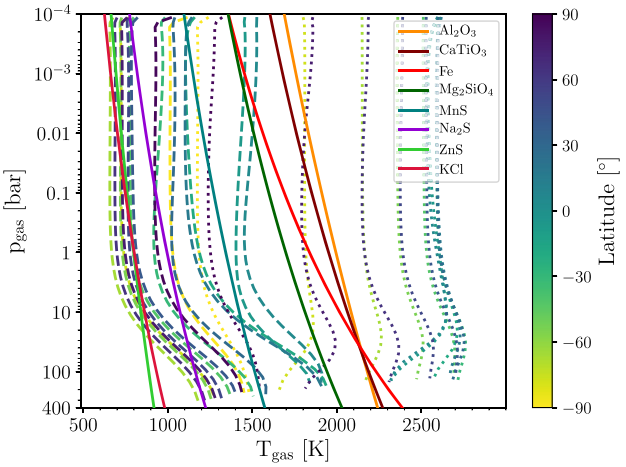

Figure 11. *T–p* profiles from −90° to 90° latitude (colour bar) at a longitude of 0° (dotted lines) and 180° (dashed lines). Coloured solid lines denote the supersaturation zones of various mineral species at solar metallicity (Lodders & Fegley 2002; Visscher, Lodders & Fegley 2006, 2010; Morley et al. 2012; Wakeford et al. 2017).

7 SUMMARY AND CONCLUSIONS

Short-period WD–BD binary systems offer a unique opportunity to explore irradiated atmospheres under more extreme conditions than typical HJ systems. In this study, we presented an initial exploration of the 3D atmospheric properties of the BD WD 0137−349B. We utilized the Exo-FMS GCM model with a dual-band grey radiative transfer scheme to model the thermal and dynamical properties of the BD atmosphere. We used the 3D radiative transfer model CMCRT to post-process the GCM output and produce synthetic emission spectra and phase curves.

Our modelling efforts suggest the atmosphere exhibits a combination of the dynamical properties expected from theory and previous (ultra)HJ studies, from the strong irradiation, high surface gravity, and short rotation period of the BD. Our results are summarized as follows.

(i) A large day–night contrast is seen in the GCM as expected from theory.

(ii) Generally inefficient day–night energy transport, except near the equatorial jet region.

(iii) Generally weak vertical velocities with overturning structures on the western terminator regions.

(iv) Phase curve shapes are generally well fit, but the absolute flux is overpredicted by a factor of ≈1–3 dependent on the photometric band.

(v) Photochemistry produces a significantly ionized upper atmospheric region.

Future modelling efforts can improve on the accuracy of our presented model with a few additions.

(i) Extending the simulation boundaries to the deeper, optically thick atmospheric regions.

(ii) Modelling the effect of UV photochemical products and radiative heating on the thermal structures in 3D.

(iii) Inclusion of a cloud formation and radiative feedback scheme.

Current and future photometric and spectroscopic instrumentation presents an exciting opportunity to observe WD 0137−349B and other WD–BD short-period binary systems in more precise detail. Such data would help further constrain the unique atmospheric properties of objects in this dynamical and radiative parameter regime, and test the theory and modelling of these objects to widen a holistic understanding of irradiated atmospheres in general.

ACKNOWLEDGEMENTS

We thank the reviewer for constructive advice and suggestions on the manuscript content. We thank V. Parmentier for advice on dynamical regime scales. GKHL thanks J. Barstow for NEMESIS formatted *k*-tables and members of the UK exoplanet community for discussion and encouragement on this project. S-M. Tsai thanks P. Rimmer for advice on compiling ion reactions. GKHL acknowledges support from the University of Oxford and CSH Bern through the Bernoulli fellowship. SLC acknowledges funding from the STFC Ernest Rutherford Fellowship program. KLC acknowledges funding from the European Union's Horizon 2020 Research and Innovation Programme, under Grant Agreement 776403. MH acknowledges support through the STFC studentship program. Plots were produced using the community open-source PYTHON packages MATPLOTLIB (Hunter 2007), SCIPY (Jones et al. 2001), and ASTROPY (Astropy Collaboration et al. 2018). Our local HPC support at Oxford is highly acknowledged. This work was supported by European Research Council Advanced Grant EXOCONDENSE (#740963).

DATA AVAILABILITY

All simulation output data are available from the lead author upon request.

REFERENCES

Allard N. F., Kielkopf J. F., Allard F., 2007, European Phys. J. D, 44, 507
Amundsen D. S., Tremblin P., Manners J., Baraffe I., Mayne N. J., 2017, A&A, 598, A97
Asplund M., Grevesse N., Sauval A. J., Scott P., 2009, ARA&A, 47, 481
Astropy Collaboration et al., 2018, AJ, 156, 123
Baes M., Gordon K. D., Lunttila T., Bianchi S., Camps P., Juvela M., Kuiper R., 2016, A&A, 590, A55
Baudino J.-L., Mollière P., Venot O., Tremblin P., Bézard B., Lagage P.-O., 2017, ApJ, 850, 150
Beuermann K. et al., 2013, A&A, 558, A96
Bordwell B., Brown B. P., Oishi J. S., 2018, ApJ, 854, 8
Burleigh M. R., Hogan E., Dobbie P. D., Napiwotzki R., Maxted P. F. L., 2006, MNRAS, 373, L55
Burleigh M. R. et al., 2011, in Schuh S., Drechsel H., Heber U., eds, AIP Conf. Proc. Vol. 1331, Planetary Systems Beyond the Main Sequence: Proceedings of the International Conference. Am. Inst. Phys., New York, p. 262
Carone L., Keppens R., Decin L., 2015, MNRAS, 453, 2412
Carone L. et al., 2020, MNRAS, 496, 3582
Casewell S. L. et al., 2012, ApJ, 759, L34
Casewell S. L. et al., 2015, MNRAS, 447, 3218
Casewell S. L. et al., 2018a, MNRAS, 476, 1405
Casewell S. L., Littlefair S. P., Parsons S. G., Marsh T. R., Fortney J. J., Marley M. S., 2018b, MNRAS, 481, 5216
Chubb K. L., Min M., Kawashima Y., Helling C., Waldmann I., 2020, A&A, 639, A3
Dobbie P. D., Burleigh M. R., Levan A. J., Barstow M. A., Napiwotzki R., Hubeny I., 2005, A&A, 439, 1159
Drummond B. et al., 2018, ApJ, 855, L31
Drummond B. et al., 2020, A&A, 636, A68
Farihi J., Christopher M., 2004, AJ, 128, 1868
Farihi J., Parsons S. G., Gänsicke B. T., 2017, Nat. Astron., 1, 0032
Fromang S., Leconte J., Heng K., 2016, A&A, 591, A144
Gill A. E., 1980, Q. J. R. Meteorological Soc., 106, 447
Guillot T., 2010, A&A, 520, A27
Hammond M., Pierrehumbert R. T., 2017, ApJ, 849, 152
Heng K., Showman A. P., 2015, Annu. Rev. Earth Planet. Sci., 43, 509
Heng K., Frierson D. M. W., Phillipps P. J., 2011, MNRAS, 418, 2669
Hernández Santisteban J. V. et al., 2016, Nature, 533, 366
Hubeny I., 1988, Comput. Phys. Commun., 52, 103
Hubeny I., Lanz T., 1995, ApJ, 439, 875
Hunter J. D., 2007, Comput. Sci. Eng., 9, 90
Irwin P., 2009, Giant Planets of Our Solar System: Atmospheres, Composition, and Structure. Springer-Verlag, Berlin
Jones E. et al., 2001, SciPy: Open Source Scientific Tools for Python. Available at: http://www.scipy.org/
Kataria T., Showman A. P., Lewis N. K., Fortney J. J., Marley M. S., Freedman R. S., 2013, ApJ, 767, 76
Kataria T., Sing D. K., Lewis N. K., Visscher C., Showman A. P., Fortney J. J., Marley M. S., 2016, ApJ, 821, 9
Komacek T. D., Showman A. P., 2016, ApJ, 821, 16
Komacek T. D., Tan X., 2018, Res. Notes Am. Astron. Soc., 2, 36
Komacek T. D., Showman A. P., Tan X., 2017, ApJ, 835, 198
Kramida A., Ralchenko Y., Reader J., 2013, NIST Atomic Spectra Database (version 5). National Institute of Standards and Technology, Gaithersburg, MD
Lacis A. A., Oinas V., 1991, J. Geophys. Res., 96, 9027
Lavvas P., Koskinen T., Yelle R. V., 2014, ApJ, 796, 15
Lee G. K. H., Wood K., Dobbs-Dixon I., Rice A., Helling Ch., 2017, A&A, 601, A22
Lee G. K. H., Taylor J., Grimm S. L., Baudino J.-L., Garland R., Irwin P. G. J., Wood K., 2019, MNRAS, 487, 2082
Lewis N. K., Showman A. P., Fortney J. J., Marley M. S., Freedman R. S., Lodders K., 2010, ApJ, 720, 344
Li G., Gordon I. E., Rothman L. S., Tan Y., Hu S.-M., Kassi S., Campargue A., Medvedev E. S., 2015, ApJS, 216, 15
Lin S.-J., 2004, Mon. Weather Rev., 132, 2293
Littlefair S. P. et al., 2014, MNRAS, 445, 2106
Liu B., Showman A. P., 2013, ApJ, 770, 42
Lodders K., Fegley B., 2002, Icarus, 155, 393
Longstaff E. S., Casewell S. L., Wynn G. A., Maxted P. F. L., Helling C., 2017, MNRAS, 471, 1728
Lothringer J. D., Barman T., Koskinen T., 2018, ApJ, 866, 27
Matsuno T., 1966, J. Meteorological Soc. Jpn. Ser. II, 44, 25
Maxted P. F. L., Napiwotzki R., Dobbie P. D., Burleigh M. R., 2006, Nature, 442, 543
Mayne N. J. et al., 2014, A&A, 561, A1
Mendonça J. M., Tsai S.-m., Malik M., Grimm S. L., Heng K., 2018, ApJ, 869, 107
Menou K., 2020, MNRAS, 493, 5038
Miles B. E. et al., 2020, AJ, in press (arXiv:2004.10770)
Morley C. V., Fortney J. J., Marley M. S., Visscher C., Saumon D., Leggett S. K., 2012, ApJ, 756, 172
Moses J. I. et al., 2011, ApJ, 737, 15
Parmentier V., 2014, PhD thesis, Laboratoire Joseph-Louis Lagrange (LAGRANGE), Université Nice Sophia Antipolis (UNS); Observatoire de la Côte d'Azur CNRS: UMR7293
Parsons S. G. et al., 2017, MNRAS, 471, 976
Penn J., Vallis G. K., 2017, ApJ, 842, 101
Penn J., Vallis G. K., 2018, ApJ, 868, 147
Pierrehumbert R. T., Ding F., 2016, Proc. R. Soc. Lond. Ser. A, 472, 20160107
Polyansky O. L., Kyuberis A. A., Zobov N. F., Tennyson J., Yurchenko S. N., Lodi L., 2018, MNRAS, 480, 2597
Rappaport S. et al., 2017, MNRAS, 471, 948
Rauscher E., Kempton E. M. R., 2014, ApJ, 790, 79
Rauscher E., Menou K., 2012, ApJ, 750, 96
Rimmer P. B., Helling C., 2016, ApJS, 224, 9
Rothman L. S. et al., 2010, J. Quant. Spectrosc. Radiat. Transf., 111, 2139
Showman A. P., Guillot T., 2002, A&A, 385, 166
Showman A. P., Polvani L. M., 2011, ApJ, 738, 71
Showman A. P., Cooper C. S., Fortney J. J., Marley M. S., 2008, ApJ, 682, 559
Showman A. P., Fortney J. J., Lian Y., Marley M. S., Freedman R. S., Knutson H. A., Charbonneau D., 2009, ApJ, 699, 564
Showman A. P., Lewis N. K., Fortney J. J., 2015, ApJ, 801, 95
Sing D. K. et al., 2019, AJ, 158, 91
Skrutskie M. F. et al., 2006, AJ, 131, 1163
Steele P. R., Burleigh M. R., Dobbie P. D., Jameson R. F., Barstow M. A., Satterthwaite R. P., 2011, MNRAS, 416, 2768
Steele P. R. et al., 2013, MNRAS, 429, 3492
Steinrueck M. E., Parmentier V., Showman A. P., Lothringer J. D., Lupu R. E., 2019, ApJ, 880, 14
Tan X., Komacek T. D., 2019, ApJ, 886, 26
Tan X., Showman A. P., 2020, preprint (arXiv:2001.06269)
Tennyson J. et al., 2016, J. Mol. Spectrosc., 327, 73
Thorngren D., Gao P., Fortney J. J., 2019, ApJ, 884, L6
Tsai S.-M., Lyons J. R., Grosheintz L., Rimmer P. B., Kitzmann D., Heng K., 2017, ApJS, 228, 20
Visscher C., Lodders K., Fegley B., Jr, 2006, ApJ, 648, 1181
Visscher C., Lodders K., Fegley B., Jr, 2010, ApJ, 716, 1060
Wakeford H. R., Visscher C., Lewis N. K., Kataria T., Marley M. S., Fortney J. J., Mandell A. M., 2017, MNRAS, 464, 4247
Witte S., Helling C., Hauschildt P. H., 2009, A&A, 506, 1367
Witte S., Helling C., Barman T., Heidrich N., Hauschildt P. H., 2011, A&A, 529, A44
Woitke P., Helling C., Hunter G. H., Millard J. D., Turner G. E., Worters M., Blecic J., Stock J. W., 2018, A&A, 614, A1
Yates J. S., Palmer P. I., Manners J., Boutle I., Kohary K., Mayne N., Abraham L., 2020, MNRAS, 492, 1691
Yurchenko S. N., Barber R. J., Tennyson J., 2011, MNRAS, 413, 1828
Yurchenko S. N., Amundsen D. S., Tennyson J., Waldmann I. P., 2017, A&A, 605, A95

APPENDIX A: G-ORDINATE EMISSION COMPOSITE BIASING

In Lee et al. (2019) a method for using the correlated *k* approximation was presented for computing emission spectra in a Monte Carlo radiative transfer context. This used an unbiased sampling for the g-ordinate of each photon packet, $g_{\rm samp}$, emitted in each cell, given by

$$g_{\rm samp} = \frac{w_{\rm g} L_{\rm g}}{\sum_{\rm g} w_{\rm g} L_{\rm g}}, \tag{A1}$$

where $w_{\rm g}$ is g-ordinate weight and $L_{\rm g}$ (erg s^{-1} cm^{-1}) the luminosity contributed by that *k*-coefficient in a cell. This scheme has the property that the higher numbered g-ordinate will usually be more likely to be sampled, since generally $w_{\rm g}L_{\rm g} < w_{\rm g+1}L_{\rm g+1}$, unless the opacity distribution is flat. In some bands where the opacity distribution has a large gradient, for example near a line centre, the lower g-ordinates may be undersampled, leading to unwanted noise by not sampling the true opacity distribution adequately.

To alleviate this we follow a composite biasing scheme similar to Baes et al. (2016) where the g-ordinate is sampled from a the unbiased probability distribution function, $p(g)$, and a uniform distribution function, $q(g)$, given by

$$q_\star(g) = (1-\xi)p(g) + \xi q(g) = \frac{(1-\xi)w_{\rm g}L_{\rm g}}{\sum_{\rm g} w_{\rm g}L_{\rm g}} + \frac{\xi}{N_{\rm g}}, \tag{A2}$$

where $N_{\rm g}$ is the number of *k*-coefficients in the band, and $\xi = [0,1]$ the composite biasing factor. The weight of the photon packet is then

$$W_{\rm ph} = \frac{1}{(1-\xi) + \xi\langle L_{\rm g}\rangle / w_{\rm g}L_{\rm g}}, \tag{A3}$$

where

$$\langle L_{\rm g}\rangle = \frac{\sum_{\rm g} w_{\rm g}L_{\rm g}}{N_{\rm g}}. \tag{A4}$$

This paper has been typeset from a TEX/LATEX file prepared by the author.